Published online 30 March 2020

Nucleic Acids Research, 2020, Vol. 48, No. 9 ***4769–4779***
doi: 10.1093/nar/gkaa192

Molecular architecture of the DNA-binding sites of the P-loop ATPases MipZ and ParA from *Caulobacter crescentus*

Laura Corrales-Guerrero[1,†], Binbin He[1,†], Yacine Refes[1,†], Gaël Panis[2], Gert Bange[3,4], Patrick H. Viollier[2], Wieland Steinchen[3,4,*] and Martin Thanbichler[1,3,5,*]

[1]Department of Biology, University of Marburg, D-35043 Marburg, Germany, [2]Department of Microbiology and Molecular Medicine, University of Geneva Medical School, CH-1211 Geneva, Switzerland, [3]Center for Synthetic Microbiology, D-35043 Marburg, Germany, [4]Department of Chemistry, University of Marburg, D-35043 Marburg, Germany and [5]Max Planck Fellow Group Bacterial Cell Biology, Max Planck Institute for Terrestrial Microbiology, D-35043 Marburg, Germany

Received December 19, 2019; Revised February 18, 2020; Editorial Decision March 06, 2020; Accepted March 17, 2020

ABSTRACT

The spatiotemporal regulation of chromosome segregation and cell division in *Caulobacter crescentus* is mediated by two different P-loop ATPases, ParA and MipZ. Both of these proteins form dynamic concentration gradients that control the positioning of regulatory targets within the cell. Their proper localization depends on their nucleotide-dependent cycling between a monomeric and a dimeric state and on the ability of the dimeric species to associate with the nucleoid. In this study, we use a combination of genetic screening, biochemical analysis and hydrogen/deuterium exchange mass spectrometry to comprehensively map the residues mediating the interactions of MipZ and ParA with DNA. We show that MipZ has non-specific DNA-binding activity that relies on an array of positively charged and hydrophobic residues lining both sides of the dimer interface. Extending our analysis to ParA, we find that the MipZ and ParA DNA-binding sites differ markedly in composition, although their relative positions on the dimer surface and their mode of DNA binding are conserved. In line with previous experimental work, bioinformatic analysis suggests that the same principles may apply to other members of the P-loop ATPase family. P-loop ATPases thus share common mechanistic features, although their functions have diverged considerably during the course of evolution.

INTRODUCTION

P-loop ATPases play a central role in the subcellular organization of bacterial cells. They are evolutionarily related to the Ras-like GTPase superfamily (1,2) and characterized by a conserved nucleotide-binding pocket containing a deviant Walker A motif (known as the P-loop) and a Walker B motif, required for ATP binding and hydrolysis (3). The members of this family share significant sequence and structural similarity and dimerize in an ATP-dependent manner (4,5). Moreover, they typically show a dynamic behavior *in vivo* that often involves changes in their localization patterns during the course of the cell cycle (6–10). Many P-loop ATPases act as spatial regulators that orchestrate cellular processes by controlling the subcellular positioning of macromolecular structures (7,11). The prototypical ParA homologs, for instance, mediate the partitioning of sister chromosomes and plasmids during cell division (9,12). Several other members of this family (MipZ, MinD, PldP and PomZ) ensure proper division site placement by controlling the polymerization of the cell division protein FtsZ into the cytokinetic FtsZ ring (6,8,13–17). Other functions of ParA-like ATPases include carboxysome segregation (McdA) (18), the positioning of chemoreceptor clusters (ParC and PpfA) (19,20) and DNA translocation during conjugation (VirC1) (21).

Caulobacter crescentus possesses two well-characterized P-loop ATPases, ParA and MipZ, which work together to coordinate chromosome segregation and cell division in this species. The functions of these two proteins are closely linked through their common interaction partner ParB, a DNA-binding protein that recognizes a cluster of centromere-like sites (*parS*) in the origin-proximal region of the chromosome (22–26). At the start of the cell cycle,

*To whom correspondence should be addressed. Tel: +49 6421 2821809; Email: thanbichler@uni-marburg.de
Correspondence may also be addressed to Wieland Steinchen. Tel: +49 6421 28 25761; Email: wieland.steinchen@synmikro.uni-marburg.de
†The authors wish it to be known that, in their opinion, the first three authors should be regarded as Joint First Authors.

the origin region is anchored at the old pole through an interaction between ParB and the polarity factor PopZ, with traces of FtsZ from the previous division event at the new pole (27,28). At the beginning of S-phase, the *parS* cluster is duplicated, and one of the ParB•*parS* complexes is rapidly moved to the opposite pole and tethered to a new patch of PopZ, in an active process driven by ParA (6,29–31). MipZ interacts dynamically with the two pole-associated ParB complexes and thus forms a bipolar gradient, with its concentration being highest at the poles and lowest at the cell center (6,13). Since it acts as an inhibitor of FtsZ polymerization, the arrival of the moving ParB•*parS*•MipZ complex leads to the disintegration of the polar FtsZ assembly, and the released FtsZ molecules, along with newly synthesized ones, assemble into a Z-ring at midcell (6).

Both ParA and MipZ establish dynamic polar gradients, based on their ability to alternate between an ADP-bound monomeric and an ATP-bound dimeric state with distinct interaction patterns and diffusion rates, in a manner controlled locally by the ParB•*parS* complexes. Although the ATPase cycles of the two proteins are based on similar principles, differences in the regulatory effect of ParB lead to clearly distinct localization behaviors. In the case of ParA, ParB acts as an ATPase-activating protein. ParA–ATP dimers remain associated with the nucleoid until they interact with a moving ParB•*parS* complex, which triggers their disassembly into monomers that are released from the DNA (19,29,31–35). Repeated cycles of ParB binding and ATP hydrolysis thus lead to a gradual shortening of the ParA gradient, thereby promoting the directional movement of ParB across the nucleoid towards one of the cell poles. For MipZ, by contrast, the polar ParB•*parS* complexes serve as catalysts that recruit monomers and facilitate their dimerization, possibly by increasing their local concentration at the cell poles (6). Newly formed MipZ dimers have DNA-binding activity and are retained in the polar regions through association with the nucleoid (6,13). Their lifetime is limited only by the low intrinsic ATPase activity of MipZ, which eventually generates monomers that return to the ParB•*parS* complexes, thereby restarting the cycle. As a result, MipZ forms stable bipolar gradients whose minimum at the cell center marks the site of cell division.

Various P-loop ATPases were shown to interact with the nucleoid to slow down their diffusion and thus enable the maintenance of subcellular protein gradients (13,18,19,36). Their non-specific DNA-binding activity was suggested to be mediated by positively charged amino acids that are exposed on the protein surface (4,20,37,38). Consistent with this idea, *in vivo* and *in vitro* studies of the *Bacillus subtilis* ParA homolog Soj (*Bs*ParA) identified two surface-exposed arginine residues that are essential for its interaction with DNA (37). Residues homologous to these arginines were later also implicated in the DNA-binding activity of PpfA from *Rhodobacter sphaeroides* (20) and PomZ from *Myxococcus xanthus* (17). More evidence for the importance of positively charged amino acids has recently come from the crystal structures of ParA–DNA complexes formed by ParA homologs from *Helicobacter pylori* (*Hp*ParA) (39) and *Sulfolobus solfataricus* pNOB8 (40), which each identified several surface-exposed lysine residues that are in direct contact with the phosphate backbone of the DNA ligand. However, the binding interface of pNOB8 ParA was clearly distinct from that of its *H. pylori* homolog, suggesting that ParA proteins could have evolved different modes of DNA binding. Notably, in addition to their non-specific DNA-binding activity, plasmid-encoded ParA homologs often possess a second DNA-binding domain that interacts specifically with sequence motifs in the *parA* promoter region to control protein homeostasis (41,42).

So far, the precise location of the DNA-binding interface of MipZ has remained unknown, because the residues contacting DNA in ParA-like P-loop ATPases are not conserved in this protein. In this study, we identify and characterize nine surface-exposed residues surrounding the dimer interface of MipZ that are critical for DNA binding. Most of them are positively charged, suggesting that MipZ interacts with DNA non-specifically by contacting the phosphate backbone. Consistent with this notion, ChIP-Seq analysis reveals that MipZ interacts with a large number of chromosomal sites without a clear preference for a specific consensus sequence. Determining the DNA-binding residues of *C. crescentus* ParA (*Cc*ParA), we further demonstrate that MipZ and ParA bind DNA in similar, positively charged regions, although the nature of the interacting residues varies considerably. Thus, while the biological functions of ParA-like ATPases have diverged significantly during the course of evolution, the general principle underlying their DNA-binding activity appears to be conserved.

MATERIALS AND METHODS

Bacterial strains and plasmids and growth conditions

The bacterial strains, plasmids and oligonucleotides used in this work are listed in Tables S1–S3. Their construction and the growth conditions used are detailed in the Supplementary information. All plasmids were verified by DNA sequencing.

Protein purification

Escherichia coli Rosetta(DE3)pLysS was transformed with suitable pET21a(+) derivatives (Table S2) and grown aerobically in LB medium. At an OD_{600} of 0.6, the medium was supplemented with 1 mM IPTG to induce protein overproduction, and the cultivation was continued for another 3 h. The cells were harvested by centrifugation, snap-frozen in liquid nitrogen and stored at −80°C until further use. To purify MipZ or its mutant derivatives, cells were thawed on ice and resuspended in a 3–5-fold volume of buffer B3 (50 mM NaH_2PO_4, 300 mM NaCl, 20 mM imidazole, 1 mM β-mercaptoethanol, pH 8.0), supplemented with 100 μg/ml PMSF (phenylmethylsulfonyl fluoride) and 10 U/ml DNase I. Afterwards, they were lyzed by two passages through a French press at 16 000 psi. Cell debris was removed by centrifugation at 30 000 × g for 30 min. The supernatant was passed through a 0.2 μm filter (Sarstedt, Germany) and then loaded onto a 5 ml HisTrap column (GE Healthcare, USA) connected to an ÄKTA Purifier 10 system (GE Healthcare). After a wash of the column with buffer B3, protein was eluted with linear gradient of imidazole (20–250 mM in a buffer containing 50 mM NaH_2PO_4 and 300

mM NaCl, pH8). The eluate was collected in fractions and subjected to SDS-PAGE. Fractions containing the protein of interest were combined and dialyzed twice against 3 L of buffer B6 (50 mM HEPES/NaOH pH 7.2, 50 mM NaCl, 5 mM $MgCl_2$, 0.1 mM EDTA, 10% glycerol). Finally, the protein solution was centrifuged at 30 000 × g for 30 min to remove precipitates, snap-frozen in liquid nitrogen and stored at −80°C. ParA-His_6 was purified as described above for MipZ-His_6, using a previously described buffer system (29).

Hydrogen-deuterium exchange mass spectrometry (HDX-MS)

MipZ-D42A or wild-type ParA (50 μM) were incubated for 15 min at room temperature with 1 mM ATPγS in the absence or presence of a 14 bp-long dsDNA oligonucleotide (ran14-up/ran14-lo; 50 μM). Subsequently, samples were prepared for HDX-MS essentially as described previously (48,49), aided by a robotic autosampler (LEAP Technologies, USA). To start the H/D exchange, 7.5 μl (50 μM) of MipZ-D42A were mixed with 67.5 μl of D_2O-containing MipZ-buffer (50 mM HEPES/NaOH pH 7.2, 50 mM NaCl, 5 mM $MgCl_2$, 0.1 mM EDTA, 1 mM ATPγS). For ParA, 7.5 μl (50 μM) of protein solution were mixed with 67.5 μl of D_2O-containing ParA-buffer (25 mM HEPES/KOH pH 7.4, 50 mM potassium glutamate, 450 mM KCl, 1 mM $MgSO_4$, 1 mM DTT, 1 mM ATPγS). After incubation for 15/30/60/120/600 s at 25°C, samples (55 μl) were taken from the reactions and mixed with 55 μl of quench buffer (400 mM KH_2PO_4/H_3PO_4, 2 M guanidine–HCl, pH 2.2), cooled to 1°C. 95 μl of the mixture were immediately injected into an ACQUITY UPLC M-class system with HDX technology (Waters, USA) (50). Proteins were digested online with immobilized pepsin at 12°C with a constant flow (100 μl/min) of water + 0.1% (v/v) formic acid, and the resulting peptic peptides were collected for 3 min on a C18 column (Waters) that was kept at 0.5°C. The trap column was then placed in line with an ACQUITY UPLC BEH C18 1.7 μm 1.0 × 100 mm column (Waters), and the peptides were eluted at 0.5°C using a gradient of water + 0.1% (v/v) formic acid (eluent A) and acetonitrile + 0.1 (v/v) % formic acid (eluent B) at a flow rate of 30 μl/min as follows: 0–7 min/95–65% A, 7–8 min/65–15% A, 8–10 min/15% A, 10–11 min/5% A, 11–16 min/95% A. Mass spectra of deuterated samples were acquired in High Definition MS positive ion mode using a G2-Si HDMS mass spectrometer equipped with an ESI source (Waters). Non-deuterated samples were prepared in the same way by incubation in non-deuterated buffer, with mass spectra recorded in Enhanced High Definition MS mode (51,52). Continuous lock mass correction was performed using a [Glu1]-Fibrinopeptide B standard (Waters). All measurements were performed in triplicate. After each run, the pepsin column was washed three times with 80 μl of 4% (v/v) acetonitrile and 0.5 M guanidine–HCl. Additionally, blank runs were performed between each analysis to avoid peptide carry-over. The identification and assignment of peptides was carried out as previously described (48,49) using PLGS and DynamX 3.0 software (Waters).

ATPase assays

ATPase assays were performed as described before (6). In brief, MipZ-His_6 or its variants (6 μM) were preincubated for 10 min at 30°C in buffer P (50 mM HEPES/NaOH pH 7.2, 50 mM KCl, 10 mM $MgCl_2$, 1 mM β-mercaptoethanol). The reaction was started by the addition of 1 mM ATP containing [α-^{32}P]ATP (25 Ci/mmol) (Hartmann, Germany). Samples (2 μl) were taken every 10 min over a period of 1 h and transferred onto PEI-cellulose F thin-layer chromatography plates (Merck, Germany). The plates were developed in a solvent system containing 1 M LiCl and 0.5 M formic acid, air-dried, and exposed to a phosphor screen (GE Healthcare, USA). After scanning of the screen in a Storm 840 PhosphorImager (GE Healthcare, Germany), the amount of [α-^{32}P]ADP in the samples was quantified using ImageQuant 5.2 (GE Healthcare). The reaction rates were determined by linear-regression analysis in Microsoft Excel 2010.

Electrophoretic mobility shift assay

Proteins (10 μM) were incubated for 15 min at room temperature with 10 nM *Eco*RI-linearized plasmid pMCS-2 (53) in EMSA buffer (10 mM HEPES/NaOH pH 7.2, 150 mM NaCl, 10 mM $MgCl_2$, 0.05% Tween 20) containing 0.46 mM ATPγS. After the addition of sample buffer, protein–DNA complexes were separated from free plasmid DNA by electrophoresis in a 1% agarose gel, prepared in TAE buffer (20 mM Tris/HCl pH 8.0, 0.175% acetic acid, 0.5 mM EDTA, pH 8.0). DNA was stained with ethidiumbromide and detected in a UV-Transilluminator (UniEquip, Germany).

Biolayer interferometry

Biolayer interferometric analyses were performed using a BLItz System (PALL Life Sciences, USA). Biotinylated ds-DNA oligonucleotides (37.5 μM) (Eurofins MWG Operon, Germany) were captured on a High Precision Streptavidin Biosensor (PALL Life Sciences). Subsequently, they were probed with wild-type MipZ or one of its mutant variants (4 μM) in buffer B6 (50 mM HEPES/NaOH pH 7.2, 50 mM NaCl, 5 mM $MgCl_2$, 0.1 mM EDTA, 10 % glycerol) containing 1 mM ATPγS. After the association step, the biosensors were transferred into buffer B6 to monitor the dissociation of the protein–DNA complexes.

RESULTS

Identification of DNA-binding residues on the MipZ surface

Our knowledge of the determinants mediating the non-specific DNA-binding activity of P-loop ATPases is largely based on studies of canonical ParA homologs. However, for this group of proteins, two distinct modes of DNA binding, mediated by different regions of the dimer surface, have been reported (39,40). Moreover, the residues identified in previous studies are not universally conserved among DNA-binding members of the P-loop ATPase family. To clarify which regions of MipZ mediate the interaction with DNA, we devised a reverse genetics approach. Taking advantage of the crystal structure of the MipZ dimer (PDB

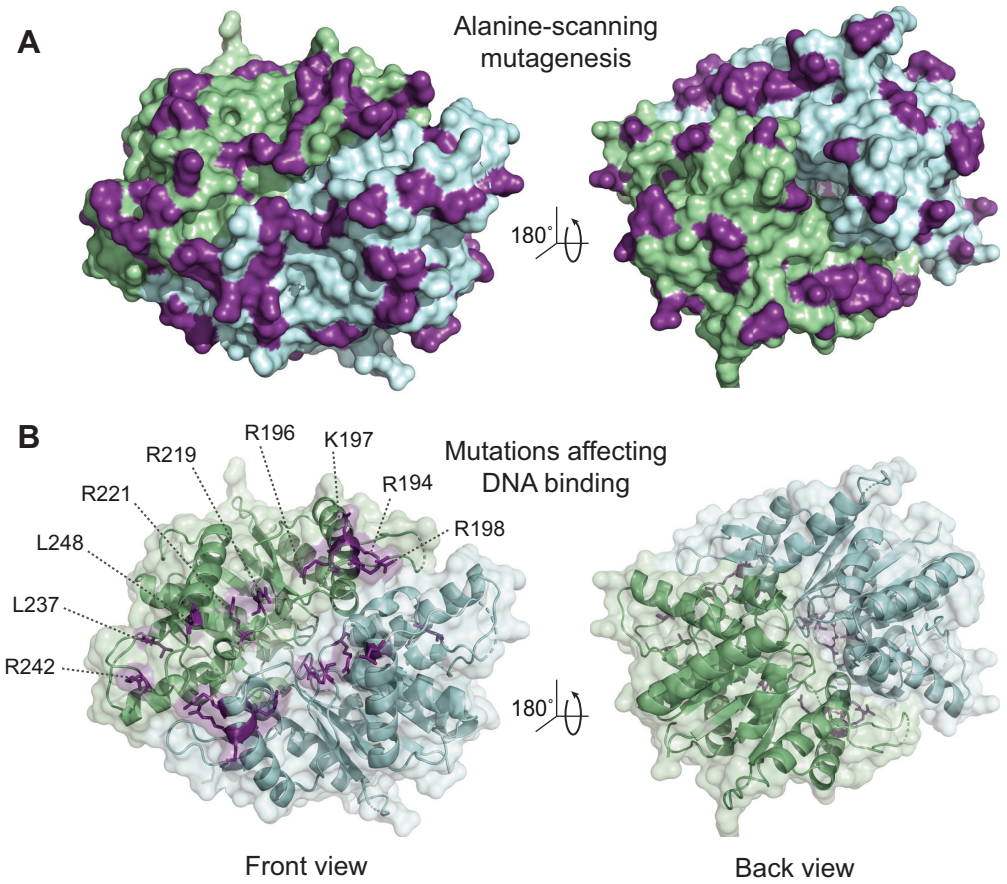

Figure 1. Identification of residues critical for DNA binding by MipZ. (**A**) Surface representation of the MipZ dimer structure (PDB ID: 2XJ9) with the 51 amino acids selected for alanine-scanning mutagenesis marked in purple. The two subunits are depicted in green and blue, respectively. (**B**) Cartoon representation of the MipZ dimer structure with nine candidate amino acids possibly involved in DNA binding shown in purple. A surface representation of the structure is shown in the background. For clarity, the ATP molecules and Mg^{2+} ions sandwiched between the two subunits are not shown.

ID: 2XJ9) (13), we selected a variety of charged or bulky hydrophobic residues that are exposed on the MipZ surface (Figure 1A) and exchanged them for alanine. The resulting 51 single-mutant MipZ variants were then analyzed for their function *in vivo*. To this end, the mutant alleles were fused to *eyfp* (encoding yellow fluorescent protein) and expressed from an inducible promoter in cells depleted of the native MipZ protein. Subsequently, the morphology of the strains and the localization patterns of the mutant proteins were determined by microscopy. As a reference, this analysis also included a wild-type MipZ-eYFP fusion, a monomeric variant (K13A) unable to interact with DNA and FtsZ, and a constitutively dimeric variant (D42A) that is locked in the DNA-binding and FtsZ-inhibitory state (6,13).

As shown previously (6,13), cells producing wild-type MipZ-eYFP displayed normal morphologies and the characteristic unipolar or bipolar gradient, indicating that the fusion protein was fully functional (Supplementary Figures S1 and S2). Expression of the K13A variant yielded a mixture of short and elongated cells as well as a high level of uniform cytoplasmic fluorescence, combined with distinct foci reflecting the positions of the ParB•*parS* complexes. The dimeric variant (D42A), by contrast, gave rise to filamentous cells showing patchy, nucleoid-associated fluorescence throughout the cell (Supplementary Figures S1 and S2).

DNA binding restrains the diffusion of MipZ and is a prerequisite for gradient formation (6). MipZ variants that fail to interact with DNA should still be able to associate with ParB. However, the dimers released from ParB should no longer be retained in the vicinity of the ParB•*parS* complexes but diffuse freely within the cytoplasm. As a consequence, they should inhibit cell division throughout the cell, leading to cell filamentation. Based on this hypothesis, we searched for mutant strains that still formed ParB-associated foci but displayed elevated levels of cytoplasmic fluorescence, combined with an increase in cell length. A total of nine strains showed the predicted phenotype (Figure 1B, Supplementary Figures S1 and S2A). The stability of the different MipZ-eYFP variants was verified by immunoblot analysis (Supplementary Figure S3A). Expression of the R194A, R196A, R198A or R221A variants led to severe filamentation, whereas strains producing the K197A, R219A, L237A, R242A or L248A variants showed a milder phenotype with a broad distribution of cell lengths (Supplementary Figure S2A). Notably, the R196A, R219A and L248A variants produced very faint ParB-associated foci, suggesting that they have an additional defect in ParB

binding (Supplementary Figure S1). An analysis of the subcellular distribution of the different MipZ-YFP variants confirmed a partial to complete loss of the gradient pattern (Supplementary Figure S2B). Interestingly, the nine amino acids identified in the screen are mostly positively charged and grouped in the same surface region, forming an extended patch that lines the dimer interface (Figure 1B).

Diffusional properties of MipZ variants with DNA-binding defects

Previous work has shown that MipZ dimers have a very low diffusion rate, likely due to their interaction with the nucleoid. Monomers, by contrast, are highly mobile, because they are rapidly exchanged between ParB•*parS* complexes and able to move freely within the cytoplasm (13). To corroborate that the newly identified variants have a reduced DNA-binding activity *in vivo*, we investigated the diffusional properties of two representative proteins (K197A and R198A) in fluorescence recovery after photobleaching (FRAP) assays. When one of the polar foci was bleached in cells showing a bipolar gradient of wild-type MipZ-eYFP, fluorescence was recovered with a half-time ($t_{1/2}$) of 9.4 ± 0.4 s (Supplementary Figure S4A). The monomeric K13A variant, by contrast, showed considerably faster kinetics ($t_{1/2} = 2.0 \pm 0.2$ s), indicating largely unrestrained diffusion (Supplementary Figure S4B). Notably, intermediate recovery rates were measured for both the K197A ($t_{1/2} = 5.6 \pm 0.2$ s) and the R198A variants ($t_{1/2} = 5.3 \pm 0.8$ s) (Supplementary Figure S4C and D). These results suggest that the two proteins are indeed less stably associated with the nucleoid and therefore diffuse more rapidly within the cell than the wild-type protein. However, they appear to interact with DNA to some extent, suggesting that they still display some residual DNA-binding activity (as confirmed below).

Biochemical characterization of the DNA-binding-deficient MipZ variants

To confirm that the phenotypes observed are indeed due to a defect in DNA binding, we overproduced and purified the nine MipZ variants selected in the mutant screen and analyzed their biochemical properties *in vitro* (Supplementary Figure S3B). Initially, we aimed to test whether the proteins were still able to undergo ATP-dependent dimerization. However, previous work has shown that the direct detection of MipZ dimers is technically challenging (13). We therefore resorted to ATPase activity measurements as a proxy, based on the fact that dimerization is a prerequisite for nucleotide hydrolysis (6,13). In all cases, the ATP turnover rates were similar to that of the wild-type protein (Figure 2A), confirming that the mutations did not affect the ATPase cycle of MipZ. By contrast, and as expected (6), the monomeric (K13A) and dimeric (D42A) variants showed very low activity levels.

Next, we tested the DNA-binding capacity of the different variants using an electrophoretic mobility shift assay (Figure 2B). For this purpose, the proteins were incubated with a linearized plasmid in the presence of the non-hydrolysable ATP analogue adenosine-5′-O-(3-thio)triphosphate (ATPγS), which locks MipZ in its

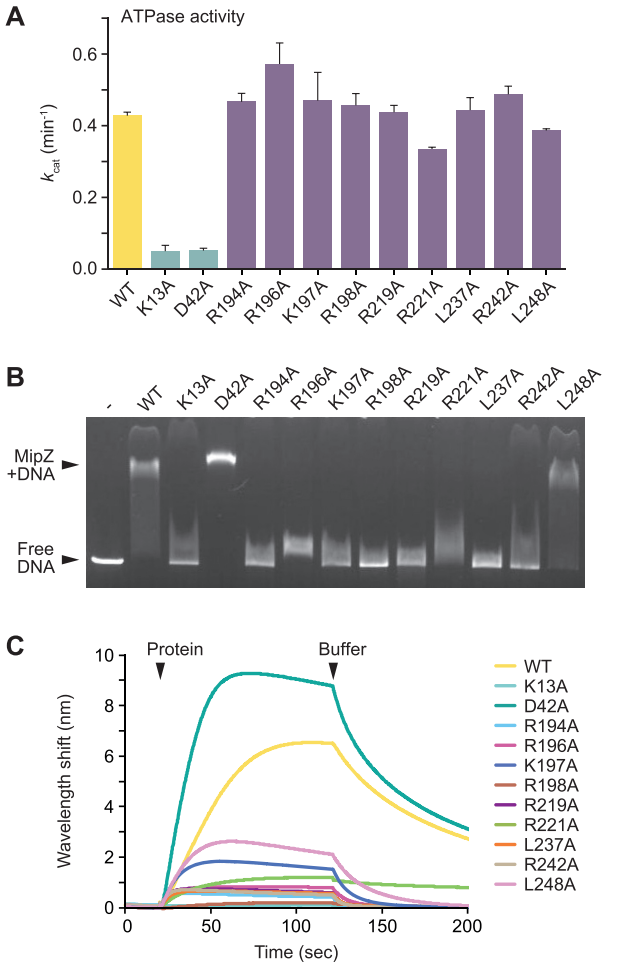

Figure 2. *In vitro* characterization of MipZ variants with DNA-binding defects. (**A**) ATPase activities of purified wild-type MipZ and the indicated mutant derivatives. MipZ (6 μM) was incubated with ATP (1 mM), and the rate of hydrolysis was determined. Shown are the average turnover numbers (k_{cat}) (±SD) from at least three independent experiments. (**B**) Electrophoretic mobility shift assay analyzing the interaction of different MipZ variants with a linearized plasmid (pMCS-2). MipZ (WT) or the indicated variants (10 μM) were incubated with DNA (10 nM) and ATPγS (0.46 mM). Protein-DNA complexes were then separated from free DNA by standard agarose gel electrophoresis. (**C**) Biolayer interferometric analysis of the DNA-binding activity of different MipZ variants. A biotinylated ds-DNA oligonucleotide (rand-biotin/rand-rev; 37.5 μM) was immobilized on the sensor surface and probed with MipZ (WT) or the indicated variants (4 μM) in the presence of ATPγS (1 mM). All analyses were performed at least three times, and representative results are shown.

dimeric state. Whereas the wild-type protein and the D42A variant strongly reduced the mobility of the DNA fragment during electrophoresis, most of the other mutant proteins showed hardly any binding activity. A slight shift was still observed for the R196A and R221A variants, while the L248A exchange hardly affected the behavior of MipZ in this assay. To corroborate these results, we additionally performed biolayer interferometric analyses. To this end, a double stranded (ds) 26 bp oligonucleotide was immobilized on a sensor chip and probed with wild-type MipZ or its mutant variants (Figure 2C). The wild-type and D42A proteins again interacted strongly with DNA. The other

mutant variants, by contrast, showed a moderate to severe decrease in the DNA-binding activity. An estimate of the changes in affinities was obtained by microscale thermophoresis experiments, in which a constant concentration of fluorescently (Cy3-) labeled dsDNA oligonucleotide was titrated with increasing concentrations of protein (Supplementary Figure S5). The data obtained enabled us to categorize the different MipZ variants into three groups: high-affinity binding proteins (K_D < 10 μM) (WT, D42A, L248A), low-affinity binding proteins (K_D >> 10 μM) (K13A, R196A, K197A, R219A, L237A, R242A) and proteins hardly showing any binding (R194A, R198A, R221A). Collectively, our *in vitro* results demonstrate that all MipZ variants selected in the mutant screen are defective in their interaction with DNA. Notably, the severity of the phenotypes observed for the different mutant strains correlates with the DNA-binding affinities of the proteins they produce, underscoring the importance of DNA binding for proper MipZ function.

MipZ binds DNA in a sequence-independent manner *in vivo*

Among the nine DNA-binding residues identified, seven are positively charged. The interaction of MipZ with DNA may therefore largely rely on electrostatic forces between positively charged MipZ residues and the negatively charged DNA phosphate backbone, as suggested for other ParA-like proteins (4,20). Consistent with this hypothesis, MipZ indeed interacts non-specifically with DNA *in vitro* (13) (see also Figure 2). However, it remained unclear whether it could have a preference for certain sequence motifs *in vivo*. To address this issue, we performed chromatin immunoprecipitation followed by high-throughput sequencing (ChIP-Seq) analysis on *C. crescentus* strains that produced a wild-type MipZ-eYFP fusion or the corresponding K13A and D42A variants in place of the native MipZ protein (Dataset S1). As expected, the monomeric K13A variant was highly enriched around the *parS* sites, with its distribution largely reflecting the binding profile of ParB (Supplementary Figure S6). The dimeric D42A variant, by contrast, was barely associated with the *parS* region. These results corroborate the previous finding that only monomeric MipZ species are efficiently recruited to the ParB•*parS* complex *in vivo* (6). Analyzing the interaction of the three fusion proteins with origin-distal chromosomal regions (Figure 3A and Dataset S1), we did not detect any clear signals for the K13A variant, in line with its limited DNA-binding activity. The same was true for the wild-type fusion, likely because only a fraction of the protein is in the DNA-binding-competent, dimeric state and its ATPase activity greatly reduces the residence time of dimers on the DNA. By contrast, a clear interaction with the nucleoid was observed for the D42A variant. Analysis of the precipitated DNA fragments revealed that it was associated with a large number of different loci (Figure 3A and Dataset S1). However, we did not observe distinct, localized signals, but broad peaks covering several kilobases of chromosomal DNA, suggesting that MipZ does not recognize defined sequence motifs. Interestingly, the extent of DNA binding was positively correlated with the GC content of the interacting chromosomal regions (Figure 3A). However, *in vitro* binding studies

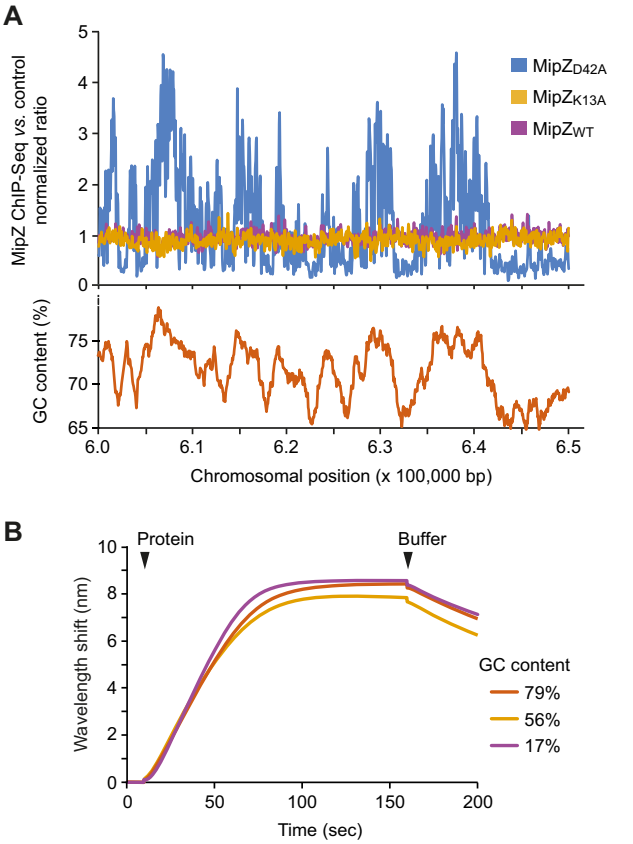

Figure 3. Global distribution of chromosomal MipZ binding sites. (**A**) ChIP-seq analysis of the distribution of different MipZ variants across the *C. crescentus* chromosome. Cells producing a wild-type (BH64), monomeric (K13A; BH100) or dimeric (D42A; BH99) MipZ-eYFP fusion in place of the native protein were fixed with formaldehyde and subjected to ChIP-seq analysis with an anti-GFP antibody. A representative 50 kb window of the chromosome is shown for visualization. Data were normalized using wild-type strain NA1000 as a reference. (**B**) Biolayer interferometric analysis of the interaction of MipZ with DNA of different GC content. Biotinylated dsDNA oligonucleotides with GC contents of 17% (ATrich-biotin/ATrich-rev), 56% (GC56-biotin/GC56-rev) or 79% (GCrich-biotin/GCrich-rev) were immobilized on biosensors and probed with wild-type MipZ (4 μM) in the presence of ATPγS (1 mM).

did not provide any evidence for an intrinsic preference of MipZ for GC-rich DNA (Figure 3B). It has been shown that many nucleoid-associated proteins from *C. crescentus*, such as HU or GapR, are enriched in AT-rich chromosomal regions (43–45). Furthermore, AT-rich sequences are typically found in the promoter regions of genes, which are heavily occupied by RNA polymerase or regulatory proteins. MipZ may therefore bind to DNA in a sequence-independent manner but, due to its moderate binding affinity, be restricted to less densely occupied, GC-rich regions.

Direct detection of the MipZ DNA-binding interface by HDX analysis

Using reverse genetics, we identified nine surface-exposed amino acid residues that are critical for the DNA-binding activity of MipZ. To verify the direct involvement of these residues in the interaction with DNA, we mapped the DNA-binding interface of MipZ by hydrogen/deuterium

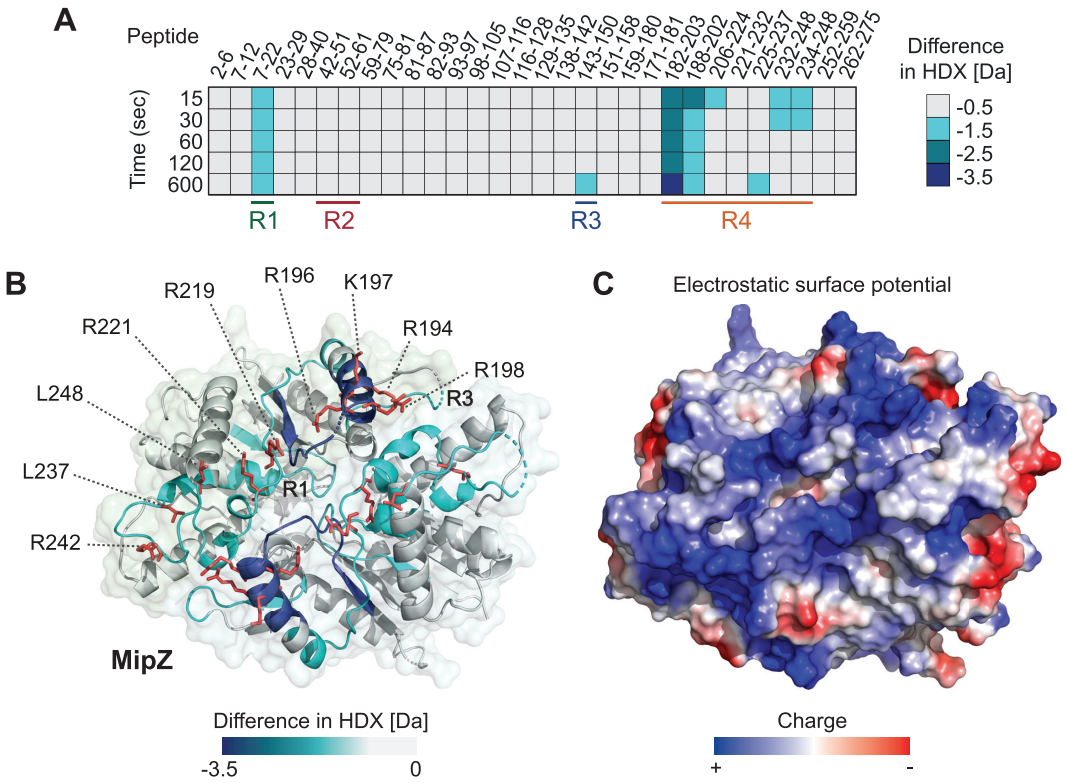

Figure 4. Hydrogen/deuterium exchange (HDX) analysis of the MipZ-DNA interaction. (**A**) MipZ-D42A was incubated in deuterated buffer containing 1 mM ATPγS in the absence or presence of a 14 bp dsDNA oligonucleotide (ran14-up/ran14-lo). The heat plot shows the maximal differences in deuterium uptake between the DNA·MipZ-D42A complex and MipZ-D42A alone at different incubation times for a series of representatives peptides (see Dataset S2 for the full list of peptides). The color code is given on the right. All experiments were performed in the presence of ATPγS to further increase the stability of the dimer. The four different regions that are protected upon DNA binding to MipZ or ParA (see Figure 5) are indicated at the bottom. (**B**) Mapping of the maximum differences in HDX observed upon DNA binding onto the crystal structure of the MipZ dimer (PDB ID: 2XJ9). The color code is given at the bottom. The DNA-binding residues identified in the mutant screen are shown in red. A surface representation of the structure is shown in the background. For clarity, the ATP and Mg^{2+} ligands are not shown. (**C**) Electrostatic surface potential of the MipZ dimer. The color code is given at the bottom.

exchange mass spectrometry (HDX-MS), a method detecting local shifts in the accessibility of backbone amide hydrogens caused by ligand binding (46). To this end, the dimeric D42A variant was transferred into deuterated buffer and incubated with or without a short (14 bp) dsDNA oligonucleotide. After fragmentation and mass spectrometric analysis of the protein, we then searched for peptides that showed a reduced rate of deuterium uptake in the presence of DNA. A total of 168 peptides were unambiguously identified, covering 94% of the protein sequence. Protected peptides mapped to three distinct regions (R1, R3, and R4) of MipZ (Figure 4A, B and Supplementary Figure S7A). A closer inspection of the data showed that R1 corresponds to the Walker A motif, suggesting a conformational change in this region upon DNA binding. R3 is only partially exposed on the dimer surface, and mutations in this region (D147A, T150A, E152A) do not affect the biological function of MipZ (Supplementary Figure S8). This region may therefore also be subject to conformational changes upon DNA binding but not directly contribute to the interaction (see also Supplementary Figure S12). The elements constituting R4, by contrast, are located on the dimer surface and contain all of the residues identified in the mutant screen (Figure 4B), confirming the relevance of the *in vivo* results. Together, these findings support the hypothesis that the DNA-binding interface of MipZ is formed by a linear array of positively charged amino acids (Figure 4C) that mediate non-specific DNA binding through interaction with the DNA phosphate backbone.

MipZ and ParA share a similar DNA-binding region

MipZ and ParA share the ability to interact non-specifically with DNA. Previously, two arginine residues at the dimer interface of ParA were shown to be critical for DNA binding (30,37). Moreover, a recent crystallographic study has suggested that *Hp*ParA interacts with DNA in a region homologous to the DNA-binding interface of MipZ (39). However, a comprehensive analysis of the determinants that mediate the ParA–DNA interaction in solution is still missing. To address this issue, we extended our HDX studies to the ParA homolog of *C. crescentus* and mapped the regions of the protein that were protected upon interaction with a dsDNA oligonucleotide (Figure 5A). Since it was not possible to purify an ATPase-deficient (D44A) variant of ParA in soluble form, the experiments were performed with the wild-type protein, locked in the dimeric state by addition of ATPγS. In total, 78 peptides were unambiguously

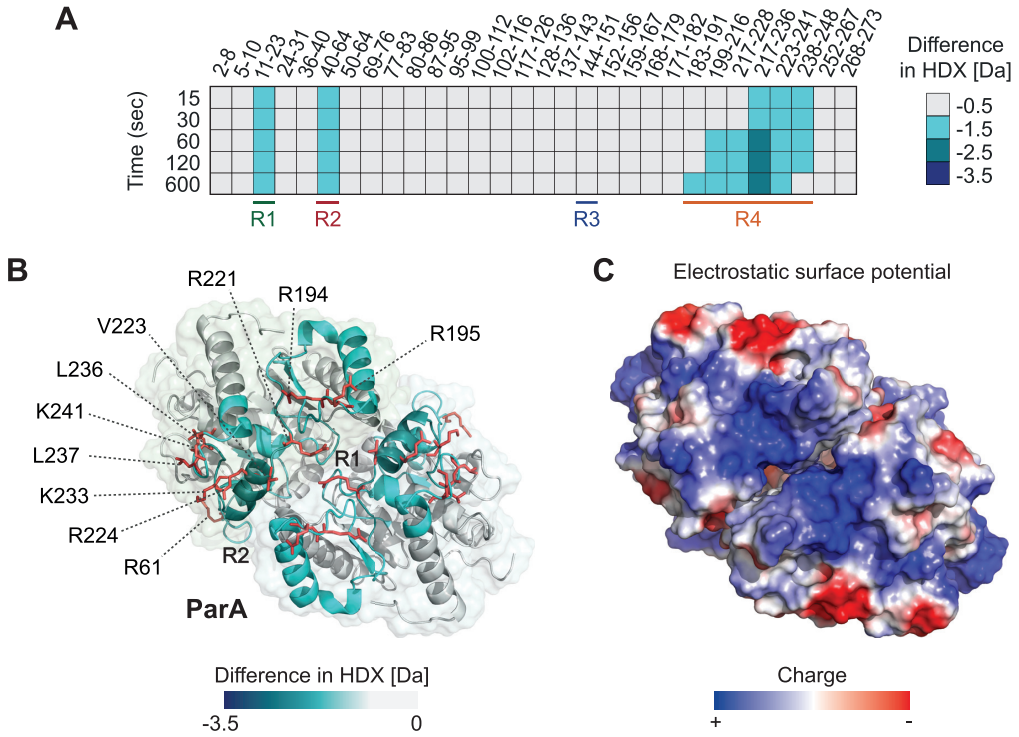

Figure 5. Hydrogen/deuterium exchange (HDX) analysis of the *C. crescentus* ParA–DNA interaction. (**A**) ParA was incubated in deuterated buffer containing 1 mM ATPγS in the absence or presence of a 14 bp dsDNA oligonucleotide (ran14-up/ran14-lo). The heat plot shows the maximal differences in deuterium uptake between the DNA·ParA complex and MipZ alone at different incubation times for a series of representatives peptides (see Dataset S2 for the full list of peptides). The color code is given on the right. All experiments were performed in the presence of ATPγS to lock the protein in the dimeric state. The four different regions that are protected upon DNA binding to MipZ (see Figure 4) or ParA are indicated at the bottom. (**B**) Mapping of the maximum differences in HDX observed upon DNA binding onto a structural model of ParA, generated with *Hp*ParA (PDB ID: 6IUB) (39) as a template. A surface representation of the structure is shown in the background. For clarity, the ATP and Mg^{2+} ligands are not shown. (**C**) Electrostatic surface potential of the ParA dimer. The color code is given at the bottom.

identified, which covered 94% of the complete protein sequence. Interestingly, out of the three protected regions, two (R1 and R4) were homologous to regions protected upon DNA binding in MipZ, whereas one (R2) was specifically detected in ParA (Figure 5A, B and Supplementary Figure S7B). The elements constituting R2 are mostly buried in the interior of the ParA dimer, suggesting that they do not directly contribute to DNA binding. Notably, however, they also include a loop with an arginine residue (R61) that is exposed on the lateral side of the complex. As in MipZ, R4 showed the highest degree of protection. It stretches along the edge of the dimer interface and includes six positively charged and two bulky hydrophobic residues that are located at the protein surface (Figure 5B, C). Consistent with a role of these residues in DNA binding, their substitution led to dissipation of the ParA gradient *in vivo*, causing origin segregation defects and aberrant cell divisions events, likely induced by the mislocalization of MipZ (Supplementary Figure S9). In line with previous work (37,39), these findings demonstrate that the DNA-binding activity of ParA also relies on non-specific electrostatic interactions with the DNA phosphate backbone. Interestingly, however, none of the residues identified in ParA has a direct equivalent in the DNA-binding pocket of MipZ, and some of the DNA-interacting residues of MipZ are located in an insertion that is not conserved in other P-loop ATPases (Figure 6). The DNA-binding determinants of the two proteins thus differ considerably, even though the principal mechanism of target recognition is identical in both cases.

DISCUSSION

In this work, we used a combination of biochemical and genetic approaches to identify and comprehensively analyze the DNA-binding sites of the P-loop ATPases MipZ and ParA from *C. crescentus*. Our results show that both proteins associate with DNA in a sequence-independent manner through electrostatic interactions with the phosphate backbone (Figure 6A). However, despite this similarity in the mechanism of action, the amino-acid composition of the binding sites varies considerably. Interestingly, most P-loop ATPases studied to date share the DNA-binding region of ParA (4,20,37–39) (Figure 6B). The interaction determinants of MipZ, by contrast, are clearly distinct and, in part, located in a segment of the protein that is not conserved in other family members. This divergence in the DNA-binding interfaces may be a result of adaptive evolution that serves to change the kinetics of the binding reaction or the effect of DNA on the ATPase cycle of MipZ.

Our study identified a total of nine residues that critically contribute to non-specific DNA binding by MipZ (Figure 4). The individual importance of these residues ap-

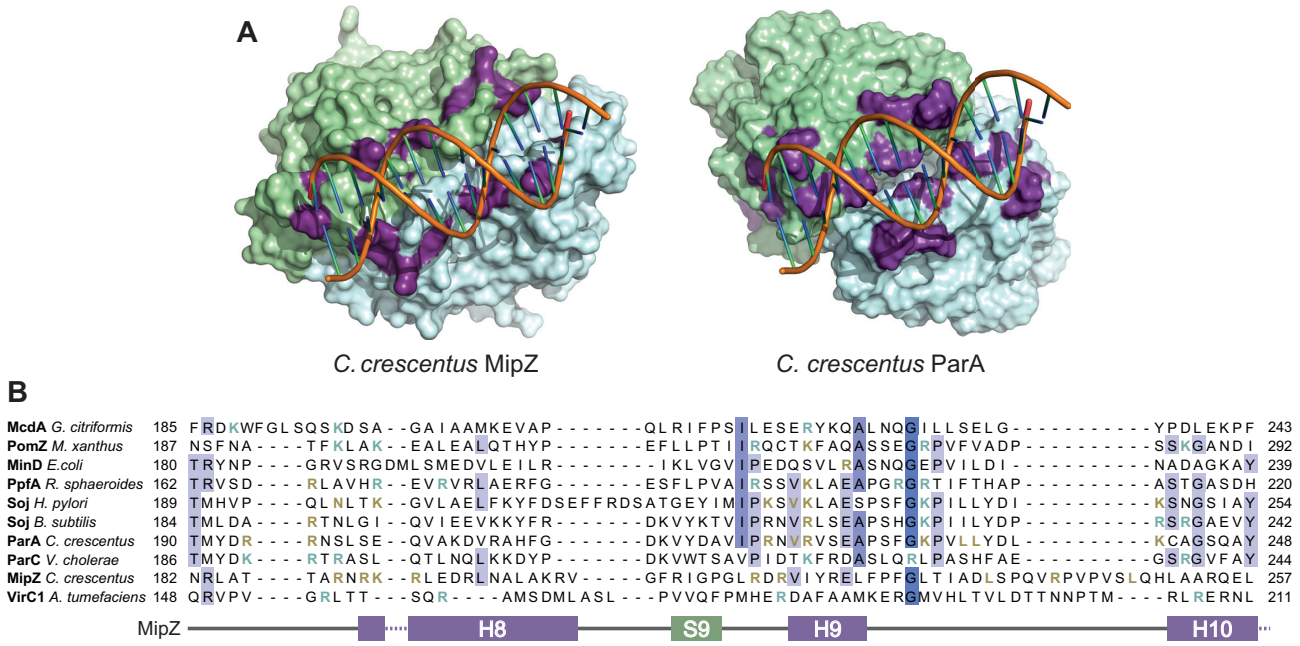

Figure 6. Variability of the DNA-binding regions of P-loop ATPases. (**A**) Comparison of the DNA-binding regions of MipZ and ParA from *C. crescentus*. Shown are surface representations of the dimer structures of MipZ (PDB ID: 2XJ9) and ParA (modeled as described in Figure 5B). Residues shown to be important for DNA binding are highlighted in purple. Short dsDNA oligonucleotides were modeled into the experimentally verified DNA-binding interfaces. The two subunits of each dimer are depicted in green and blue, respectively. (**B**) Alignment of the DNA-binding regions of the indicated P-loop ATPases (see Supplementary Figure S10 for details), corresponding to region R4 from Figures 4 and 5. Conserved residues are highlighted in blue. Residues proven to be involved in DNA-binding are colored orange. Residues predicted to have a role in DNA binding (see also Supplementary Figure S12) are shown in cyan. The corresponding secondary structural elements of MipZ from *C. crescentus* (13) are indicated at the bottom. See Supplementary Figure S10 for an alignment of the full-length sequences.

pears to differ significantly. Despite their peripheral location in the DNA-binding interface, R194 and R198 are essential for interaction with DNA, consistent with the observation that they are part of a region that is highly protected from the environment upon DNA binding. The remaining residues make additional contacts that contribute to stabilizing the MipZ-DNA interaction. Interestingly, while the majority of them are positively charged and, thus, suited to directly contact the DNA phosphate backbone, two (L237 and L248) have bulky hydrophobic side chains. Mutations in these leucines had only moderate effects on the functionality of MipZ *in vivo*, although the L237A variant showed a strongly reduced DNA-binding activity *in vitro*. The precise role of these residues remains to be investigated. Notably, the crystal structure of the *Hp*ParA–DNA complex revealed a conserved leucine residue that is in direct contact with the DNA molecule. However, this interaction involves the main chain amide group rather than the hydrophobic side chain (39). A similar situation may be observed for MipZ, with mutations in L237 and L248 leading to distortions in the main chain that impede its interaction with the phosphate backbone. Notably, residues L237, R242 and L248 are located in a loop (H9-H10) that is not found in other P-loop ATPases (Figure 6B). A structural superimposition of the MipZ dimer (13) and the *Hp*ParADNA complex (39) suggests that this loop inserts into the major groove of the interacting DNA molecule (Supplementary Figure S11), thereby providing additional contacts outside the conserved P-loop ATPase core. Interestingly, DNA binding also leads to conformational changes in the Walker A motif, thus likely affecting the kinetics of DNA hydrolysis. Consistent with this idea, previous work has shown a stimulatory effect of DNA on the ATPase activity of MipZ (13). Since the DNA-binding site of MipZ spans the dimer interface and comprises residues from both subunits, only the dimeric complex should have full DNA-binding activity. This hypothesis is supported by the observation that monomeric MipZ variants are unable to interact with DNA *in vitro* or stably associate with the nucleoid *in vivo* (13) (Figure 2). Notably, a comparison of the MipZ monomer and dimer structures shows that the DNA-binding regions undergo conformational changes upon dimerization, which may contribute to stabilizing the MipZ-DNA interaction (Supplementary Figure S12). In line with the lack of target specificity *in vitro*, ChIP-seq experiments demonstrated that MipZ does not bind to distinct chromosomal sites *in vivo*. Nevertheless, it is not evenly distributed across the nucleoid but enriched in GC-rich regions, potentially due to the influence of competing proteins that preferentially interact with AT-rich sequences. It will be interesting to see whether other ParA-like ATPases with non-specific DNA-binding activity (20,37,39,40) show a similar bias in their distribution.

Our analysis of the DNA-binding determinants of ParA identified ten positively charged or bulky hydrophobic residues (Figure 5) that are located in regions protected by DNA *in vitro* and critical for ParA function *in vivo*. Two of these residues (R195 and R224) are conserved in several other ParA-like ATPases (Figure 6B), and one or both of their counterparts have previously been implicated in the

DNA-binding activity of other ParA homologs (30,37,39), PpfA (20), and PomZ (17). Moreover, the residues equivalent to R221, V223, R224 and K241 are in direct contact with DNA in the crystal structure of *Hp*ParA (39), indicating an excellent agreement between the HDX and crystallographic data. In addition, we identified three more residues that are critical for DNA binding by *Cc*ParA (K233, L236, L237) and also conserved in other ParA homologs, suggesting that they could be core components of the DNA-binding site in members of the ParA family. By contrast, R194 of *Cc*ParA is not conserved in other ParA homologs but present in ParC.

In general, a comparison of different P-loop ATPases shows that the DNA-binding determinants are often poorly conserved (Figure 6B). However, most crystallized members of this family share a patch of positively charged residues that stretches along the dimer interface in corresponding regions of the proteins (Supplementary Figure S13). Modeling studies with *Hp*ParA as a template suggest that the same may be true for other ParA-like ATPases, such as PpfA, ParC, VirC1 and PomZ, whose structures still remain to be solved. A notable exception to this rule is the cell division regulator MinD, which was shown to interact non-specifically with DNA and thus contribute to chromosome segregation in *E. coli* (47). In this protein, the region that typically forms the DNA-binding interface shows a high density of negative charges and only contains a single arginine residue (R219), which is essential for DNA binding (47). These observations suggest that MinD may use a different mode of DNA binding than its family relatives. Interestingly, a recent crystal structure of the archaeal plasmid pNOB8 ParA-DNA complex revealed a unique mode of DNA-binding in which the ParA dimer interacts laterally with two DNA molecules (Supplementary Figure S14). In doing so, it undergoes a large conformational change, with one subunit rotating ∼38° relative to the second subunit, thereby opening the active site and exposing the sandwiched nucleotides to the solvent (40). Our HDX analysis of *Cc*ParA and MipZ did not reveal any obvious shift in the accessibility of the dimer interface upon DNA binding. Moreover, both proteins displayed only a single DNA-binding interface per dimer, located in a region that is distinct from the sites contacting DNA in the pNOB8 ParA structure (Supplementary Figure S15). In line with previous studies (37,39), we therefore suggest that P-loop ATPases typically have similar conformations in the DNA-free and complexed state and bind DNA through a single patch of positively charged residues located at the edge of the dimer interface. Collectively, our results support the notion that ParA-like ATPases represent a diverse family of regulators that share common functional principles but have diverged considerably to adapt to distinct cellular functions.

DATA AVAILABILITY

ChIP-seq raw data have been deposited to the Gene Expression Omnibus (GEO) database under accession number GSE137346 (samples numbers GSM4076063–GSM4076066 and GSM4086387). The raw data of the ParB ChIP-Seq analysis have been previously deposited to the GEO database under accession number GSE79918 (sample GSM2108314).

SUPPLEMENTARY DATA

Supplementary Data are available at NAR Online.

ACKNOWLEDGEMENTS

We thank Julia Rosum for excellent technical assistance, Daniela Kiekebusch, Till Ringel and Jaspara Knopp for help with the alanine-scanning mutagenesis, and Luis M. Oviedo for assistance with MatLab.
Author contributions: L.C.-G. generated strains, performed *in vivo* analyses and conducted the FRAP experiments. B.H. generated strains and conduced *in vivo* and *in vitro* studies. Y.R. purified the proteins and performed the biolayer interferometry analysis. G.P. performed the ChIP-Seq analysis. W.S. performed the HDX experiments. L.C.-G., B.H., Y.R., G.P., G.B., W.S. and M.T. analyzed the data. P.V. and M.T. supervised the work. L.C.-G., Y.R. and M.T. wrote the paper, with input from all other authors.

FUNDING

German Research Foundation (DFG) [269423233 – TRR 174; to G.B. and M.T.]; Swiss National Science Foundation [31003A_182576 to P.H.V.]; Max Planck Society [Max Planck Fellowship; to M.T.]; DFG Core Facility for Interactions, Dynamics and Macromolecular Assembly Structure (MIDAS) (to G.B.); L.C.-G. received funding from the Horizon Research and Innovation Program of the European Union [659174; MIPZ]. Funding for open access charge: Deutsche Forschungsgemeinschaft.
Conflict of interest statement. None declared.

REFERENCES

1. Leipe,D.D., Wolf,Y.I., Koonin,E.V. and Aravind,L. (2002) Classification and evolution of P-loop GTPases and related ATPases. *J. Mol. Biol.*, **317**, 41–72.
2. Bange,G. and Sinning,I. (2013) SIMIBI twins in protein targeting and localization. *Nat. Struct. Mol. Biol.*, **20**, 776–780.
3. Koonin,E.V. (1993) A superfamily of ATPases with diverse functions containing either classical or deviant ATP-binding motif. *J. Mol. Biol.*, **229**, 1165–1174.
4. Leonard,T.A., Butler,P.J. and Löwe,J. (2005) Bacterial chromosome segregation: structure and DNA binding of the Soj dimer – a conserved biological switch. *EMBO J.*, **24**, 270–282.
5. Cordell,S.C. and Löwe,J. (2001) Crystal structure of the bacterial cell division regulator MinD. *FEBS Lett.*, **492**, 160–165.
6. Thanbichler,M. and Shapiro,L. (2006) MipZ, a spatial regulator coordinating chromosome segregation with cell division in *Caulobacter*. *Cell*, **126**, 147–162.
7. Ebersbach,G. and Gerdes,K. (2001) The double *par* locus of virulence factor pB171: DNA segregation is correlated with oscillation of ParA. *Proc. Natl. Acad. Sci. U.S.A.*, **98**, 15078–15083.
8. Raskin,D.M. and de Boer,P.A. (1999) Rapid pole-to-pole oscillation of a protein required for directing division to the middle of *Escherichia coli*. *Proc. Natl. Acad. Sci. U.S.A.*, **96**, 4971–4976.
9. Marston,A.L. and Errington,J. (1999) Dynamic movement of the ParA-like Soj protein of *B. subtilis* and its dual role in nucleoid organization and developmental regulation. *Mol. Cell*, **4**, 673–682.
10. Quisel,J.D., Lin,D.C. and Grossman,A.D. (1999) Control of development by altered localization of a transcription factor in *B. subtilis*. *Mol. Cell*, **4**, 665–672.
11. Lutkenhaus,J. (2012) The ParA/MinD family puts things in their place. *Trends Microbiol.*, **20**, 411–418.
12. Gerdes,K., Howard,M. and Szardenings,F. (2010) Pushing and pulling in prokaryotic DNA segregation. *Cell*, **141**, 927–942.

13. Kiekebusch,D., Michie,K.A., Essen,L.O., Löwe,J. and Thanbichler,M. (2012) Localized dimerization and nucleoid binding drive gradient formation by the bacterial cell division inhibitor MipZ. *Mol. Cell*, **46**, 245–259.
14. Lutkenhaus,J. and Sundaramoorthy,M. (2003) MinD and role of the deviant Walker A motif, dimerization and membrane binding in oscillation. *Mol. Microbiol.*, **48**, 295–303.
15. Donovan,C., Schwaiger,A., Kramer,R. and Bramkamp,M. (2010) Subcellular localization and characterization of the ParAB system from *Corynebacterium glutamicum*. *J. Bacteriol.*, **192**, 3441–3451.
16. Treuner-Lange,A., Aguiluz,K., van der Does,C., Gomez-Santos,N., Harms,A., Schumacher,D., Lenz,P., Hoppert,M., Kahnt,J., Munoz-Dorado,J. *et al.* (2013) PomZ, a ParA-like protein, regulates Z-ring formation and cell division in *Myxococcus xanthus*. *Mol. Microbiol.*, **87**, 235–253.
17. Schumacher,D., Bergeler,S., Harms,A., Vonck,J., Huneke-Vogt,S., Frey,E. and Sogaard-Andersen,L. (2017) The PomXYZ proteins self-organize on the bacterial nucleoid to stimulate cell division. *Dev. Cell*, **41**, 299–314.
18. MacCready,J.S., Hakim,P., Young,E.J., Hu,L., Liu,J., Osteryoung,K.W., Vecchiarelli,A.G. and Ducat,D.C. (2018) Protein gradients on the nucleoid position the carbon-fixing organelles of cyanobacteria. *Elife*, **7**, e39723.
19. Ringgaard,S., Schirner,K., Davis,B.M. and Waldor,M.K. (2011) A family of ParA-like ATPases promotes cell pole maturation by facilitating polar localization of chemotaxis proteins. *Genes Dev.*, **25**, 1544–1555.
20. Roberts,M.A., Wadhams,G.H., Hadfield,K.A., Tickner,S. and Armitage,J.P. (2012) ParA-like protein uses nonspecific chromosomal DNA binding to partition protein complexes. *Proc. Natl. Acad. Sci. U.S.A.*, **109**, 6698–6703.
21. Atmakuri,K., Cascales,E., Burton,O.T., Banta,L.M. and Christie,P.J. (2007) *Agrobacterium* ParA/MinD-like VirC1 spatially coordinates early conjugative DNA transfer reactions. *EMBO J.*, **26**, 2540–2551.
22. Toro,E., Hong,S.H., McAdams,H.H. and Shapiro,L. (2008) *Caulobacter* requires a dedicated mechanism to initiate chromosome segregation. *Proc. Natl. Acad. Sci. U.S.A.*, **105**, 15435–15440.
23. Mohl,D.A. and Gober,J.W. (1997) Cell cycle-dependent polar localization of chromosome partitioning proteins in *Caulobacter crescentus*. *Cell*, **88**, 675–684.
24. Lin,D.C. and Grossman,A.D. (1998) Identification and characterization of a bacterial chromosome partitioning site. *Cell*, **92**, 675–685.
25. Graham,T.G., Wang,X., Song,D., Etson,C.M., van Oijen,A.M., Rudner,D.Z. and Loparo,J.J. (2014) ParB spreading requires DNA bridging. *Genes Dev.*, **28**, 1228–1238.
26. Broedersz,C.P., Wang,X., Meir,Y., Loparo,J.J., Rudner,D.Z. and Wingreen,N.S. (2014) Condensation and localization of the partitioning protein ParB on the bacterial chromosome. *Proc. Natl. Acad. Sci. U.S.A.*, **111**, 8809–8814.
27. Bowman,G.R., Comolli,L.R., Zhu,J., Eckart,M., Koenig,M., Downing,K.H., Moerner,W.E., Earnest,T. and Shapiro,L. (2008) A polymeric protein anchors the chromosomal origin/ParB complex at a bacterial cell pole. *Cell*, **134**, 945–955.
28. Laloux,G. and Jacobs-Wagner,C. (2013) Spatiotemporal control of PopZ localization through cell cycle-coupled multimerization. *J. Cell Biol.*, **201**, 827–841.
29. Lim,H.C., Surovtsev,I.V., Beltran,B.G., Huang,F., Bewersdorf,J. and Jacobs-Wagner,C. (2014) Evidence for a DNA-relay mechanism in ParABS-mediated chromosome segregation. *Elife*, **3**, e02758.
30. Ptacin,J.L., Lee,S.F., Garner,E.C., Toro,E., Eckart,M., Comolli,L.R., Moerner,W.E. and Shapiro,L. (2010) A spindle-like apparatus guides bacterial chromosome segregation. *Nat. Cell Biol.*, **12**, 791–798.
31. Vecchiarelli,A.G., Neuman,K.C. and Mizuuchi,K. (2014) A propagating ATPase gradient drives transport of surface-confined cellular cargo. *Proc. Natl. Acad. Sci. U.S.A.*, **111**, 4880–4885.
32. Scholefield,G., Whiting,R., Errington,J. and Murray,H. (2011) Spo0J regulates the oligomeric state of Soj to trigger its switch from an activator to an inhibitor of DNA replication initiation. *Mol. Microbiol.*, **79**, 1089–1100.
33. Le Gall,A., Cattoni,D.I., Guilhas,B., Mathieu-Demaziere,C., Oudjedi,L., Fiche,J.B., Rech,J., Abrahamsson,S., Murray,H., Bouet,J.Y. *et al.* (2016) Bacterial partition complexes segregate within the volume of the nucleoid. *Nat. Commun.*, **7**, 12107.
34. Surovtsev,I.V., Campos,M. and Jacobs-Wagner,C. (2016) DNA-relay mechanism is sufficient to explain ParA-dependent intracellular transport and patterning of single and multiple cargos. *Proc. Natl. Acad. Sci. U.S.A.*, **113**, E7268–E7276.
35. Shebelut,C.W., Guberman,J.M., van Teeffelen,S., Yakhnina,A.A. and Gitai,Z. (2010) *Caulobacter* chromosome segregation is an ordered multistep process. *Proc. Natl. Acad. Sci. U.S.A.*, **107**, 14194–14198.
36. Surovtsev,I.V., Lim,H.C. and Jacobs-Wagner,C. (2016) The slow mobility of the ParA partitioning protein underlies its steady-state patterning in *Caulobacter*. *Biophys. J.*, **110**, 2790–2799.
37. Hester,C.M. and Lutkenhaus,J. (2007) Soj (ParA) DNA binding is mediated by conserved arginines and is essential for plasmid segregation. *Proc. Natl. Acad. Sci. U.S.A.*, **104**, 20326–20331.
38. Volante,A. and Alonso,J.C. (2015) Molecular anatomy of ParA-ParA and ParA-ParB interactions during plasmid partitioning. *J. Biol. Chem.*, **290**, 18782–18795.
39. Chu,C.H., Yen,C.Y., Chen,B.W., Lin,M.G., Wang,L.H., Tang,K.Z., Hsiao,C.D. and Sun,Y.J. (2019) Crystal structures of HpSoj-DNA complexes and the nucleoid-adaptor complex formation in chromosome segregation. *Nucleic Acids Res.*, **47**, 2113–2129.
40. Zhang,H. and Schumacher,M.A. (2017) Structures of partition protein ParA with nonspecific DNA and ParB effector reveal molecular insights into principles governing Walker-box DNA segregation. *Genes Dev.*, **31**, 481–492.
41. Davis,M.A., Martin,K.A. and Austin,S.J. (1992) Biochemical activities of the *parA* partition protein of the P1 plasmid. *Mol. Microbiol.*, **6**, 1141–1147.
42. Mori,H., Mori,Y., Ichinose,C., Niki,H., Ogura,T., Kato,A. and Hiraga,S. (1989) Purification and characterization of SopA and SopB proteins essential for F plasmid partitioning. *J. Biol. Chem.*, **264**, 15535–15541.
43. Arias-Cartin,R., Dobihal,G.S., Campos,M., Surovtsev,I.V., Parry,B. and Jacobs-Wagner,C. (2017) Replication fork passage drives asymmetric dynamics of a critical nucleoid-associated protein in *Caulobacter*. *EMBO J.*, **36**, 301–318.
44. Ricci,D.P., Melfi,M.D., Lasker,K., Dill,D.L., McAdams,H.H. and Shapiro,L. (2016) Cell cycle progression in *Caulobacter* requires a nucleoid-associated protein with high AT sequence recognition. *Proc. Natl. Acad. Sci. U.S.A.*, **113**, E5952–E5961.
45. Swinger,K.K. and Rice,P.A. (2007) Structure-based analysis of HU-DNA binding. *J. Mol. Biol.*, **365**, 1005–1016.
46. Konermann,L., Pan,J. and Liu,Y.H. (2011) Hydrogen exchange mass spectrometry for studying protein structure and dynamics. *Chem. Soc. Rev.*, **40**, 1224–1234.
47. Di Ventura,B., Knecht,B., Andreas,H., Godinez,W.J., Fritsche,M., Rohr,K., Nickel,W., Heermann,D.W. and Sourjik,V. (2013) Chromosome segregation by the *Escherichia coli* Min system. *Mol. Syst. Biol.*, **9**, 686.
48. Pausch,P., Steinchen,W., Wieland,M., Klaus,T., Freibert,S.A., Altegoer,F., Wilson,D.N. and Bange,G. (2018) Structural basis for (p)ppGpp-mediated inhibition of the GTPase RbgA. *J. Biol. Chem.*, **293**, 19699–19709.
49. Han,X., Altegoer,F., Steinchen,W., Binnebesel,L., Schuhmacher,J., Glatter,T., Giammarinaro,P.I., Djamei,A., Rensing,S.A., Reissmann,S. *et al.* (2019) A kiwellin disarms the metabolic activity of a secreted fungal virulence factor. *Nature*, **565**, 650–653.
50. Wales,T.E., Fadgen,K.E., Gerhardt,G.C. and Engen,J.R. (2008) High-speed and high-resolution UPLC separation at zero degrees Celsius. *Anal. Chem.*, **80**, 6815–6820.
51. Geromanos,S.J., Vissers,J.P., Silva,J.C., Dorschel,C.A., Li,G.Z., Gorenstein,M.V., Bateman,R.H. and Langridge,J.I. (2009) The detection, correlation, and comparison of peptide precursor and product ions from data independent LC-MS with data dependant LC-MS/MS. *Proteomics*, **9**, 1683–1695.
52. Li,G.Z., Vissers,J.P., Silva,J.C., Golick,D., Gorenstein,M.V. and Geromanos,S.J. (2009) Database searching and accounting of multiplexed precursor and product ion spectra from the data independent analysis of simple and complex peptide mixtures. *Proteomics*, **9**, 1696–1719.
53. Thanbichler,M., Iniesta,A.A. and Shapiro,L. (2007) A comprehensive set of plasmids for vanillate- and xylose-inducible gene expression in *Caulobacter crescentus*. *Nucleic Acids Res.*, **35**, e137.